



Cite this: *RSC Adv.*, 2018, 8, 18896

# Diffusion doping route to plasmonic Si/SiO<sub>x</sub> nanoparticles†

Sergei S. Bubenov,<sup>ID</sup>\*<sup>a</sup> Sergey G. Dorofeev,<sup>ID</sup><sup>a</sup> Andrei A. Eliseev,<sup>ID</sup><sup>ab</sup> Nikolay N. Kononov,<sup>c</sup> Alexey V. Garshev,<sup>ab</sup> Natalia E. Mordvinova<sup>ID</sup><sup>ad</sup> and Oleg I. Lebedev<sup>d</sup>

Semiconductor nanoparticles (SNPs) are a valuable building block for functional materials. Capabilities for engineering of electronic structure of SNPs can be further improved with development of techniques of doping by diffusion, as post-synthetic introduction of impurities does not affect the nucleation and growth of SNPs. Diffusion of dopants from an external source also potentially allows for temporal control of radial distribution of impurities. In this paper we report on the doping of Si/SiO<sub>x</sub> SNPs by annealing particles in gaseous phosphorus. The technique can provide efficient incorporation of impurities, controllable with precursor vapor pressure. HRTEM and X-ray diffraction studies confirmed that obtained particles retain their nanocrystallinity. Elemental analysis revealed doping levels up to 10%. Electrical activity of the impurity was confirmed through thermopower measurements and observation of localized surface plasmon resonance in IR spectra. The plasmonic behavior of etched particles and EDX elemental mapping suggest uniform distribution of phosphorus in the crystalline silicon cores. Impurity activation efficiencies up to 34% were achieved, which indicate high electrical activity of thermodynamically soluble phosphorus in oxide-terminated nanosilicon.

Received 16th April 2018  
 Accepted 14th May 2018

DOI: 10.1039/c8ra03260b

[rsc.li/rsc-advances](http://rsc.li/rsc-advances)

## 1 Introduction

Dispersions of semiconductor nanoparticles (SNPs) are generally accepted as prospective semiconductor inks for low cost printable electronics including integrated field-effect transistor circuits,<sup>1,2</sup> and optoelectronic<sup>3</sup> and thermoelectric<sup>4</sup> devices. In this respect, SNP doping by controlled embedding of lattice vacancies<sup>5</sup> or impurity defects,<sup>6</sup> as well as surface functionalization with Lewis acid/base agents<sup>1</sup> is commonly employed for tuning electronic structure of SNPs. Processed materials may retain 0D nanocrystallinity,<sup>1</sup> interconnect *via* “molecular solders”,<sup>2</sup> or be entirely sintered.<sup>3,4</sup> The latter approach leads to superior values of charge carrier mobility. As semiconducting behavior is desired for the sintered layers, production of SNPs with low doping levels (DLs) of ~1 impurity per particle is of practical interest for semiconductor inks. At the same time, highly-doped SNPs have potential applications in nanoscale

photonics. SNPs containing more than ~10 free charge carriers per particle exhibit localized surface plasmon resonance (LSPR)<sup>7,8</sup> in the infrared (IR) region of the spectrum. In contrast to LSPR of nano-sized metals, the position of this feature is dynamically tunable with redox processes and charge injection. This leads to a possibility of using SNPs as electro-optic logic gates.<sup>7</sup> Thus, a broad range of impurity concentrations is desired in doped SNPs.

Among common semiconductors, silicon SNPs benefit from Earth crust abundance, non-toxicity, unique surface passivation options and advanced current level of Si technology. Generally, doping of Si SNPs is accomplished during the formation of particles either through decomposition of silane/impurity precursor mixtures<sup>4,6,9–15</sup> or through Si segregation in Si-rich glasses or oxynitride films.<sup>16–23</sup> In both cases nucleation of silicon nanoparticles occurs in strongly non-equilibrium conditions, which allows the production of hyperdoped Si SNPs. Concentrations up to 18% at were achieved in the case of phosphorus,<sup>9</sup> having maximal bulk solubility in silicon of ~0.5% at.<sup>24</sup> High impurity level affects the growth of SNPs. Decreased mean size<sup>10</sup> as well as an increase in the number of twin stacking faults<sup>10–12</sup> in hyperdoped Si SNPs has been reported previously. Twin boundaries may scatter charge carriers and thus degrade the quality of LSPR absorption peak.<sup>9</sup> Moreover, SNPs obtained by aforementioned techniques are prone to impurity segregation in case of P-doping. As much as 60–90% of impurity atoms are located at surface/interface in case of both

<sup>a</sup>Department of Chemistry, Lomonosov Moscow State University, 1-3 Leninskie Gory, Moscow 119991, Russia. E-mail: dorofeev\_sg@mail.ru

<sup>b</sup>Department of Materials Science, Lomonosov Moscow State University, 1-73 Leninskie Gory, Moscow 119991, Russia

<sup>c</sup>Prokhorov General Physics Institute, Russian Academy of Sciences, 38 Vavilov Str., Moscow 119991, Russia

<sup>d</sup>Laboratoire CRISMAT, UMR6508, CNRS-ENSICAEN, 6 Boulevard Marechal Juin, Caen 14050, France

† Electronic supplementary information (ESI) available. See DOI: 10.1039/c8ra03260b



freestanding<sup>2,10,15</sup> and embedded nanocrystals.<sup>18</sup> Low dopant activation efficiencies observed by electron spin resonance (2–5%)<sup>6</sup> and modeling of LSPR (~1%)<sup>9</sup> are often ascribed to impurity segregation. The problem may be partially related to a kinetically controlled doping regime, as substitutional doping of silicon cores by phosphorus has been shown to be thermodynamically preferable in case of hydroxyl or surface oxide passivation.<sup>25–27</sup>

The studies of post-synthetic doping of Si SNPs are rather scarce<sup>28–31</sup> and concern embedded Si nanocrystals only, those cannot be considered for industrial application. DLs up to 6% at were reported for phosphorus. The development of post-synthetic diffusion doping techniques to complement existing “one-pot” methods can provide much higher flexibility of the synthetic strategies for practical uses. Moreover thermodynamic solubility of dopants in the diffusion regime would result in high quality of the structures for effective charge carrier generation and LSPR features. Thus, here we report on the diffusion doping of freestanding Si/SiO<sub>x</sub> core/shell SNPs *via* high temperature annealing in phosphorus vapor. Obtained SNPs are readily plasmonic at higher DLs, LSPR modeling reveals that up to 34% of impurity atoms are electrically active.

## II Experimental

The reactants used were of analytical grade unless otherwise stated. Commercially available standard solutions of fluoro-silicate and phosphate were used as calibrants for chemical analysis. Distilled water was used for sol preparation, etching and analytical procedures. Nitric acid (68%) was distilled before use.

Undoped Si SNPs were synthesized by laser-induced chemical vapor deposition (CVD) using silane precursor. The details on procedure and apparatus are presented elsewhere.<sup>32</sup> After the synthesis, nanoparticles were allowed to oxidize at ambient conditions for several days. To obtain a doped sample ~100 mg of Si powder was transferred to a clean degassed quartz ampoule. Relative atomic ratio of P : Si in the synthesis was chosen as the variable parameter. Hereinafter, the quantitative composition of the samples is represented in the format of  $N_p/(N_{Si} + N_p)$  molar fraction in the nanoparticles. The compositions with phosphorus content of 0.6, 1.3, 2.5, 9.1, 20, 36% were synthesized and examined. For high phosphorus content (over 9% P) a weighted amount of red phosphorus (ultrapure) was added to the ampoule prior to its evacuation to  $10^{-5}$  bar. For lower phosphorus content, gaseous phosphine (50%, mixed with argon for safety reasons) was introduced into vacuumed volume and the quantity of phosphorus was determined from the gas pressure. The ampoules were sealed and carefully transferred to a tube furnace, where annealing proceeded for 2.5 hours at 900 °C for all samples. The pressure in the ampoules was calculated to be <1 atm at the temperature of phosphine decomposition. The change of the precursor was dictated by a considerable error introduced by weighing of <5 mg of phosphorus. Estimate of the diffusion depth of P was carried out using crystalline silicon (c-Si) diffusivity parameters at the annealing conditions.<sup>33</sup> The estimate yields a value of ~40 nm, which exceeds average Si crystallite size several times.

At the end of the procedure the ampoules were transferred to the side of the furnace and residual phosphorus was collected at the cold end of ampoules. After cooling down the powders were extracted and stored in glass vials at ambient conditions. For comparison powder of undoped SNPs was annealed *in vacuo* at 1000 °C for 5 hours.

Doped samples will be further denoted as Si<sub>x</sub>, where  $x$  is the molar fraction of phosphorus in the synthesis given in percent. Undoped SNPs will be referred to as Si<sub>0</sub>, vacuum-annealed – as Si<sub>va</sub>.

Aqueous sols of SNPs were prepared by sonication with SM3H (Sono Swiss) ultrasound bath. Initially the powder was dispersed in the ethanol/water (1 : 1) mixture to provide better wetting. Afterwards the semiconductor material was washed by water 3 times in a sedimentation (EBA centrifuge,  $2.5 \times 10^4$  g)/ultrasonic dispersion cycle. Doped SNPs were also treated with 30% nitric acid after the second sedimentation to oxidize residual elemental phosphorus, which may be present on the well developed surface of SNPs. The concentration of Si in the obtained sols equaled 4–7 mg ml<sup>-1</sup>. The sols were rather opaque due to partial agglomeration of Si nanoparticles in polar solvents.<sup>11</sup>

Wet chemical etching of SNPs was performed in a stepwise manner. 500 μl of 38% HF (chemical grade) were added to 500 μl of SNPs' sol. The etching proceeded for 5 minutes in dark to enhance SiO<sub>x</sub>/Si etching ratio. The mixture was treated with an ultrasound during the procedure, as the presence of hydronium ions coagulates aqueous sols of Si/SiO<sub>x</sub> SNPs. After that, the mixture was centrifuged ( $2.5 \times 10^4$  g) and the supernatant was discarded. In order to remove residual HF the SNPs were washed twice by water in a manner described above. The oxide layer at the surface of SNPs was then restored with ultrasonic-assisted treatment by 30% nitric acid for 10 minutes. After following sedimentation the precipitate was washed twice with water. Up to 4 steps of etching were performed for each sample.

To analyze Si content in the samples a spectrophotometric technique was used.<sup>34</sup> Prior to the analysis, powders, pellets or sols were dissolved either with addition of 2 ml of 0.2 M NaOH solution or with addition of a HF/HNO<sub>3</sub> (1 : 2) mixture. As SNPs show increased reductive reactivity, no catalyst was needed for oxidation. Chloroacetic buffer solution used in the original technique was substituted with acetic buffer of the same pH value. 320 mg of boric acid were added to each sample before analysis to suppress the interference of F<sup>-</sup> ions.<sup>34</sup> Polypropylene wares were employed for all preparative procedures, spectra were recorded in 1 cm polyacrylate cuvettes on a Cary 50 (Varian) ultraviolet-visible spectrophotometer in 300–450 nm wavelength region.

The amount of phosphorus in the samples was determined using ELAN DRC II (Perkin Elmer) mass spectrometer with inductively coupled plasma. In a typical analysis 1.5 ml of HF/HNO<sub>3</sub> (1 : 2) mixture was added to a sample, containing ~5 mg of silicon. The resultant solution was evaporated to dryness at 110 °C in perfluoroethylene chamber in air flow. This allows to eliminate most of silicon and fluorine macroelements from the solution, while concentrating phosphorus in the residue in the form of phosphate.<sup>35</sup> Solid residue was dissolved in water and analyzed.



IR spectra were recorded on a Frontier (Perkin Elmer) Fourier-transform IR spectrometer in a wavenumber range of 500–7800  $\text{cm}^{-1}$ , with 4  $\text{cm}^{-1}$  spectral resolution. The samples were analyzed either in the form of pellets obtained by pressing of powders with dry KBr, or in the form of drop-cast films on aluminium mirrors. The pellet specimens were studied using a pass-through setup, while film specimens were placed in a gas-flow chamber and studied with Diffuse-IR (Pike) diffuse reflection accessory. Degassing to 450  $^{\circ}\text{C}$  was performed in argon (99.993%) flow to avoid oxidation of SNPs during sample preparation and analysis. Ten scans were averaged to obtain each spectrum.

Raman spectra were recorded on InVia (Renishaw) Raman microscope with 514.5 nm 20 mW Ar-laser excitation. The samples were studied as liquid sols in backscattering regime in the spectral range of 200–1400  $\text{cm}^{-1}$  with a spectral resolution better than 1  $\text{cm}^{-1}$ , and 5 s per point signal acquisition.

Transmission electron microscopy (TEM), electron diffraction (ED) and high resolution TEM (HRTEM) studies were performed on FEI Tecnai G2 30 UT LaB<sub>6</sub> microscope operated at 300 kV with 0.17 nm point resolution. The energy-dispersive X-ray spectroscopy (EDX) elemental mapping and high-angle annular dark field scanning TEM (HAADF-STEM) was performed using a JEM ARM200F cold field emission gun electron microscope with probe and image aberration correction operated at 200 kV and equipped with a large solid-angle CENTURIO EDX detector and Quantum GIF. The samples were placed on copper holey carbon grids by drop-casting of sols with subsequent drying.

For thermopower measurements, the samples were vacuum dried after etching ( $10^{-3}$  bar) and pressed into pellets at 400 MPa. Nickel contacts were vapor deposited to the opposite sides of the pellets. The pellets were positioned between heated top and massive bottom copper contacts. The temperature of top contact was measured close to the sample with a Pt1000 sensor. Thermopower was registered with a high-ohmic 24-bit digital Expert-001 (Ekoniks) recorder.

X-ray diffraction (XRD) patterns were collected on a D/MAX-2500PC (Rigaku) diffractometer ( $\text{CuK}_{\alpha 1,2}$  radiation). Thermal expansion experiment was performed with Rigaku HT1500 high temperature attachment using platinum sample holder. Prior to measurements the attachment was washed three times by argon and evacuated. Registration of diffractograms was performed at  $5 \times 10^{-4}$  bar with argon inflow at a set of temperatures of 25, 150, 250, 350, 450, 550  $^{\circ}\text{C}$ . The treatment of the XRD data was carried out using Jana 2006 program package.<sup>36</sup>

### III Results and discussion

To characterize doping technique we first take an effort to decouple annealing effects from the impact of impurity incorporation. Annealing is known to cause an improvement in the quality of Si/SiO<sub>x</sub> interface<sup>13,37</sup> and speed up crystallization of amorphous silicon (a-Si).<sup>30</sup> An a-Si layer may be present on the surface of Si SNPs due to partial crystallization in CVD synthesis.<sup>10</sup> Such a layer can also appear at sub-Si/SiO<sub>x</sub> interface after oxidation due to strain.<sup>26</sup>

XRD patterns (Fig. 1) show all the reflexes corresponding to diamond Si structure (Si: ICDD number 27–1402, space group  $Fd\bar{3}m$ ,  $a = 0.357$  nm), with the intensity increased both upon vacuum-annealing and doping. This is accompanied by an increase in the mean crystallite size from 9 nm for initial Si SNPs to 12 nm for annealed and  $\sim 23$  nm for doped samples, as determined from the lines broadening with Scherrer formula. These observations may be accounted for crystallization of a-Si, with intra- or inter-particle sintering of crystallites. Notably, in all the cases diffuse reflexes of amorphous silicon oxide (at  $2\theta \approx 22^{\circ}$ ,  $36^{\circ}$ ) are present in XRD patterns, illustrating surface oxidation of particles.

Results obtained from Raman spectroscopy confirm the presence of a-Si and its crystallization with annealing. Raman spectra of SNPs samples (Fig. 1, inset) distinctively illustrate Fano-type peak positioned at  $\sim 520$   $\text{cm}^{-1}$ , corresponding to longitudinal optical (LO) – transverse optical (TO) phonon mode of Si lattice, and a lower wavenumber shoulder, which is attributed to vibrations in a-Si. The spectra are fit well by two components: an asymmetric resonance peak and a sum of two broad Gaussian components separated by 6  $\text{cm}^{-1}$ . The latter is a simplistic variation of the use of Gaussian-smeared vibrational density-of-states for c-Si accounting for scattering in a-Si.<sup>38</sup> The shoulder feature is only significant for unannealed Si SNPs, with the intensity ratio of  $\sim 0.4 : 1$  to c-Si phonon peak. Thus we can conclude that crystallization of a-Si in the nanoparticles occurs upon annealing regardless of the presence of phosphorus.

The asymmetric lineshape used in modeling of Raman spectra is given by:<sup>39</sup>

$$\alpha(\omega) = \alpha_0 \frac{(q + (\omega - \omega_{\text{PH}})/\gamma)^2}{1 + (\omega - \omega_{\text{PH}})^2/\gamma^2} \quad (1)$$

where  $\omega$  is the excitation frequency,  $\omega_{\text{PH}}$  is the phonon frequency,  $\gamma$  is the linewidth parameter,  $q$  is the asymmetry parameter and  $\alpha_0$  is the prefactor.

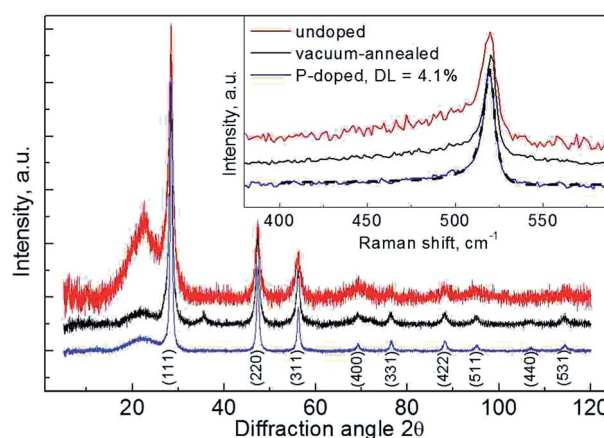


Fig. 1 XRD patterns of samples: (red) – Si<sub>0</sub>; (black) – Si<sub>va</sub>; (blue) – Si<sub>20</sub>. Inset – Raman spectra of the samples. Dashed line – result of approximation of Raman spectrum of the doped sample with asymmetric resonance curve (see eqn (1), main text). The curves are offset vertically for clarity.



This form of curve was originally derived for transitions involving mixed discrete and continual (or pseudo-continual) states<sup>40</sup> and is often used to fit Raman spectra of doped Si.<sup>6,39</sup>

Asymmetric resonance is presumed to originate from interaction between  $\Gamma$ -point optical phonons and a continuum of free carrier states.<sup>6</sup> However, at the nanoscale undoped Si also exhibits asymmetric broadening of Raman features<sup>41</sup>. Thus, a minor asymmetry effect does not readily prove the existence of free carriers. The position of LO-TO phonon mode of Si in Raman spectra is dependent on the surface-to-volume ratio, and hence on the mean crystallite size.<sup>41</sup> The size of SNPs was estimated to be  $\sim 10$  nm for all the samples with use of theoretical curve from ref. 42. This value differs significantly from the results of XRD analysis. That inconsistency, however, can be attributed to a number of parameters affecting the position of the phonon mode, including size distribution in ensemble,<sup>6,9,43</sup> impurity incorporation<sup>44</sup> and strain.<sup>45</sup>

Investigation of doped SNPs by TEM reveals agglomerates which obstruct accurate particle size determination. However, an analysis of the diffraction contrast and lattice projections allows estimation of mean diameter of SNPs to be in range of 15–30 nm (Fig. 2(a)). Corresponding ED pattern shows the presence of Si rings only, with no extra reflections provided by the impurities. This stands in agreement with XRD results. HRTEM images of individual SNPs (Fig. 2(b)) confirm their good crystallinity and structural perfection. Some of SNPs exhibit twinning structure, however the amount of such defects is much lower than reported for hyperdoped Si SNPs.<sup>10</sup> EDX elemental mapping (Fig. 2(c)) clearly illustrates localization of oxygen on the external surface of Si agglomerates, which is consistent with the formation of native silicon oxide as a result of air exposure. The thickness of this layer was estimated to be around 2 nm. The distribution of phosphorus throughout the sample is homogeneous, with minor segregation appearing at the surface of SNPs. Thus, doping of Si/SiO<sub>x</sub> SNPs was achieved by annealing in phosphorus vapor. No significant sintering of the particles was observed by experimental methods mentioned above.

As doping of silicon is realized by diffusion, time, temperature and precursor vapor pressure appear to be the control parameters of the technique. In principle, complex vapor/temperature temporal profiles can be utilized to fabricate SNPs with specific concentration and distribution of an impurity.

In this study we have first considered the effect of precursor vapor pressure. Phosphorus content in doped SNPs as obtained by elemental analysis and quantitative EDX spectroscopy is represented in Table 1.

The resulted values deviate significantly the initial composition in the reactor ampoule. Nevertheless, the specified and the obtained levels of impurity inclusion correlate well, indicating key role of precursor vapor pressure on the composition of SNPs (Fig. 3). Maximum doping level of 10% at was achieved by the method. Efficiency of dopant inclusion may likely be improved by tuning of annealing conditions.

As soon as some segregation of phosphorus was detected by EDX mapping, additional analysis was performed after HF etching of nanoparticles. Etching selectively removes SiO<sub>x</sub> layer

of core/shell Si/SiO<sub>x</sub> nanoparticles, thus, phosphorus content in the etched samples should represent doping level in silicon core. Indeed, the quantitative analysis of silicon removal efficiency by single step etching was evaluated as  $\sim 30\%$ . On the other hand a dramatic decrease in phosphorus content was detected with etching (Table 1). Moreover, phosphorus loss correlates strongly with the initial phosphorus content and attains 85% for maximal doping levels. This illustrates that segregation of phosphorus appears to SiO<sub>x</sub> layer with the efficiency increasing strongly with the impurity content. Some kind of saturation is observed at  $\sim 2\%$  of phosphorus content in the etched samples, which can be assigned to the maximum P solubility in Si SNPs.

By the very definition every spatial position in a nano-material is at most in 50 nm proximity of a surface or interface.

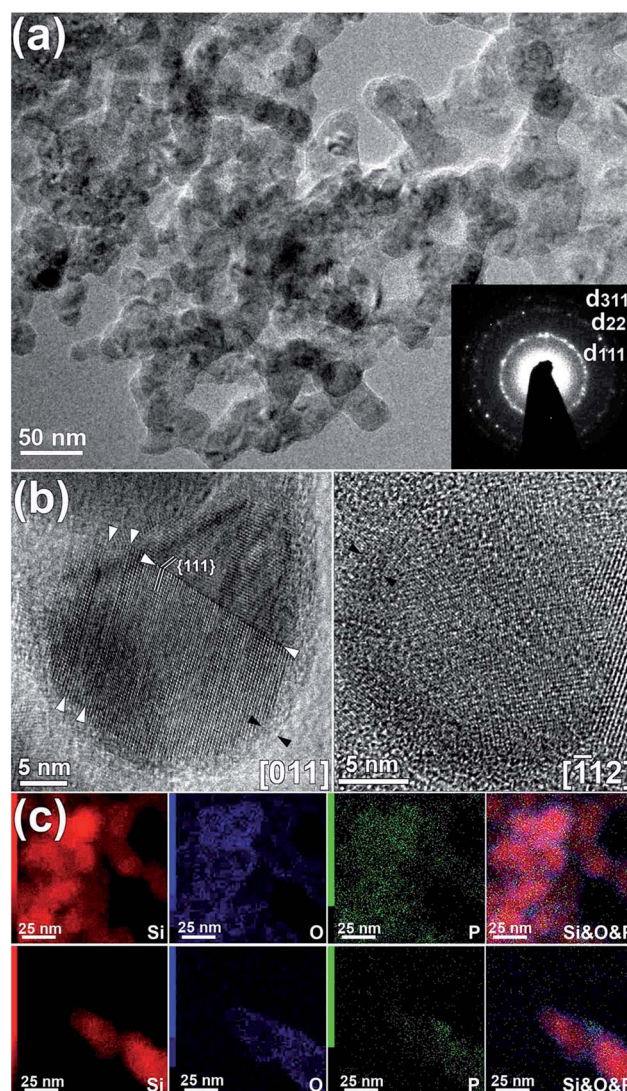


Fig. 2 TEM study of P-doped sample Si<sub>1.3</sub>: (a) low magnification bright field TEM image the inset ring ED pattern evidences Si structure. (b) bright field HRTEM images of single Si SNPs viewed along [011] and  $[-112]$  directions. Twin {111} planes are marked with white arrows. Si oxide layer is marked with black arrows. (c) EDX elemental mapping of Si K, O K, P K and overlaid color image (Si – red, O – blue, P – green).



Table 1 Composition and LSPR properties of P-doped Si SNPs

Sample	Synthesis	$N_p/(N_{Si} + N_p)$ ratio%		As synthesized			After etching		
		Total	Core	LSPR position, $\text{cm}^{-1}$	$N_c$ , $\text{cm}^{-3}$	Carrier activation efficiency	LSPR position, $\text{cm}^{-1}$	$N_c$ , $\text{cm}^{-3}$	Carrier activation efficiency
		ICP MS							
Si_0.6	0.6	0.126	0.19	—	—	—	—	—	—
Si_1.3	1.3	0.28	0.15	—	—	—	—	—	—
Si_2.5	2.5	0.44	0.29	—	—	—	—	—	—
Si_9.1	9.1	2.5	1.1	1990	$8.8 \times 10^{19}$	7.0%	2030	$9.5 \times 10^{19}$	17%
Si_20	20.0	4.1	0.95	1990	$9.1 \times 10^{19}$	4.5%	2050	$1.6 \times 10^{20}$	34%
Si_36	35.9	9.9	2.0	1840	$4.0 \times 10^{19}$	0.8%	2050	$1.3 \times 10^{20}$	13%

Thus significance of surface/interface states dramatically increases in SNPs comparing to bulk crystalline phases or disordered materials. Importantly, the hydrogenic impurities in Si can form stable complexes with dangling bonds, effectively negating the impact of both defects on the electronic structure of SNPs as it was predicted by *ab initio* calculations.<sup>25,45</sup> This compensation has experimentally been observed as an offset of an impurity influence on the conductivity<sup>6</sup> or Seebeck coefficient<sup>4</sup> of laser-annealed films made of Si SNPs. The value of the offset of  $10^{18}$  to  $10^{19} \text{ cm}^{-3}$  is consistent with the surface concentration of defects ( $10^{11}$  to  $10^{12} \text{ cm}^{-2}$ )<sup>37</sup> and surface-to-volume ratio of  $\sim 6 \times 10^6 \text{ cm}^{-1}$  (for  $\sim 10 \text{ nm}$  Si nanoparticles). It is thus imperative to probe the electrical activity of the impurity in SNPs.

The pellets made of doped SNPs illustrate a serious rise in the conductivity of at least 2 orders of magnitude as compared to the undoped sample. Results of thermoelectric measurements are given in Section S.I of the ESI.† The thermopower had a positive sign, consistent with n-type doping of silicon. Absolute values of Seebeck coefficient were established as 590, 500, 130, 170  $\mu\text{V K}^{-1}$  for Si\_0.6, Si\_1.3, Si\_2.5 and Si\_36 samples correspondingly. This generally inverse relation of Seebeck coefficient and impurity content can be explained in terms of Fermi level shift towards the conduction band and expected

linear dependence of the Seebeck coefficient on the energy difference between Fermi level and the edge of the band.<sup>4,11</sup>

In the strongly doped samples the existence of free charge carriers was confirmed independently through the observation of LSPR mode in their IR spectra (Fig. 4). The spectra include vibrations corresponding to  $\text{SiO}_x$  ( $1100$  and  $1200 \text{ cm}^{-1}$ ),  $\text{H}_2\text{O}$  and hydroxyl ( $3000$ – $3700 \text{ cm}^{-1}$ ), methyl ( $2960 \text{ cm}^{-1}$ ) and methylene ( $2860$ ,  $2930 \text{ cm}^{-1}$ ) group vibrations superimposed on a prominent LSPR band with a FWHM of  $\sim 2000 \text{ cm}^{-1}$ . Details of designation of bands to group frequencies are given in Section S.II of the ESI.†

LSPR of nanoparticles is often described in terms of Mie absorption theory for microspheres in quasi-static limit:<sup>46,47</sup>

$$\sigma(\omega) = \frac{8\pi^2 R^3 \varepsilon_M^{0.5} \omega}{c} \text{Im} \left( \frac{\varepsilon_P(\omega) - \varepsilon_M}{\varepsilon_P(\omega) + 2\varepsilon_M} \right) \quad (2)$$

where  $\sigma$  is the absorption cross section,  $R$  – the mean radius of nanoparticles,  $c$  – the speed of light,  $\varepsilon_P$  – the dielectric function of the particles,  $\varepsilon_M$  – the dielectric constant of surrounding medium. Evidently, LSPR feature is sensitive to dielectric environment. In conjunction with hygroscopicity of Si/SiO<sub>x</sub> nanoparticles ( $\sim 1\%$  wt. of H<sub>2</sub>O absorbed, as determined with quartz microbalance) this leads to the necessity of degassing of SNPs'

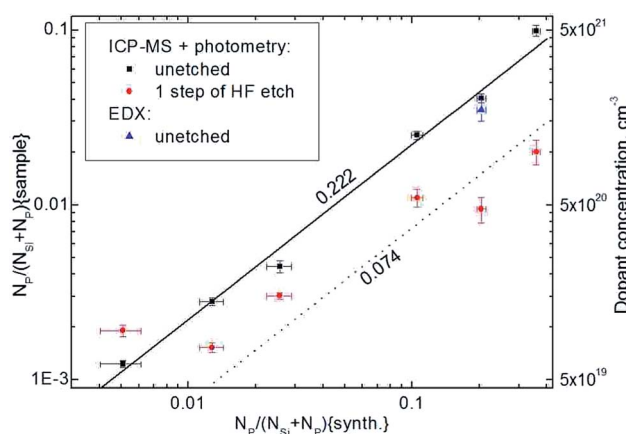


Fig. 3 Results of elemental analysis of doped SNPs: ICP-MS and photometry analysis of unetched samples (■) and samples after 1 step of HF etching (●); EDX microanalysis of unetched samples (▲). The lines, representing constant levels of impurity inclusion in SNPs, are guides for the eye.

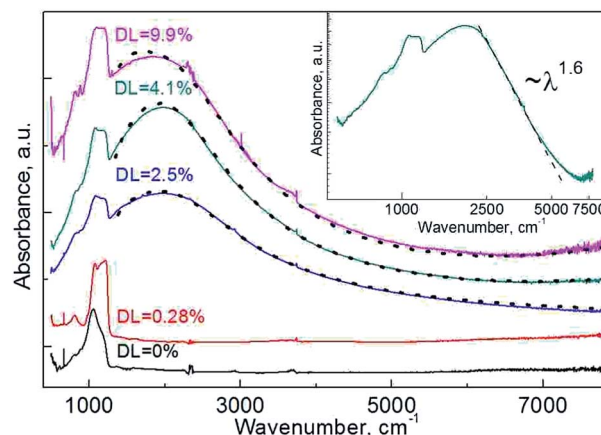


Fig. 4 IR spectra of Si SNPs samples: (black) – Si\_0; (red) – Si\_1.3; (blue) – Si\_9.1; (cyan) – Si\_20; (magenta) – Si\_36. Dotted curves – approximations of the optical response (see main text). Inset – log plot of IR spectra of sample Si\_20. Dashed line indicates the slope of linearized portion of the log plot. The curves are offset vertically for clarity.



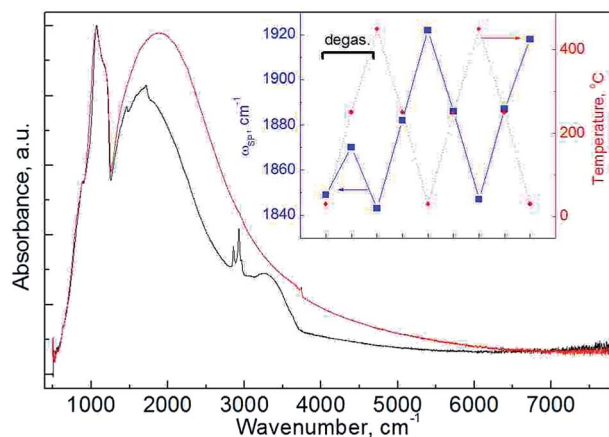


Fig. 5 The effect of degassing of plasmonic samples in argon on the form of IR spectrum: (black) – spectrum of etched sample Si\_36 prior to degassing, (red) – spectrum of the same sample after degassing. Inset – the effect of temperature on the plasmonic band: changes in position of maximum of LSPR band (■) of sample Si\_20 with temperature (●) in two heating/cooling cycles.

films in argon flow before spectrum acquisition. Indeed, the maximum of the band  $\omega_{sp}$  blueshifts, and intensity of the band improves as the signal corresponding to hydroxyl-related features drops significantly (Fig. 5). Blueshift of the position with reduced  $\epsilon_M$  proves the plasmonic nature of the broad peak.<sup>7</sup>

Dielectric function of plasmonic SNPs is frequently modeled assuming their degenerate state with use of Drude equation:

$$\epsilon_P = \epsilon_\infty - \frac{\omega_P^2}{\omega^2 + i\omega\Gamma} \quad (3)$$

where  $\epsilon_\infty$  is the high-frequency dielectric constant of SNPs,  $\omega_P$  – the plasmonic frequency of SNPs,  $\Gamma$  – the damping term,  $i$  – the imaginary unit. A combination of eqn (2) and (3) tends to adequately describe plasmonic behavior of semiconductor and metal nanoparticles. It is, however, inappropriate for the analysis of the derived data as the form of low-energy tail deviates theory significantly. Importantly,  $\alpha \sim \lambda^2$  dependence is expected for LSPR peak tails<sup>16</sup> while the samples show a flatter profile with a power of  $\sim 1.5$  (Fig. 4, inset). This corresponds to plasmon damping, which can occur through electron–electron, electron–phonon or electron–defect interaction as well as through surface scattering. When electron–electron scattering term dominates,  $\Gamma$  is frequency-independent (as in Drude model) and the plasmonic band is weakly influenced by the temperature.<sup>48</sup> In case of Si SNPs a significant and reversible redshift of  $\omega_{sp}$  occurs upon heating (Fig. 5, inset). According to thermal XRD experiment (Section S.III of the ESI†) thermal expansion of the lattice only accounts for  $\sim 0.2\%$  drop in  $\omega_P$ . Major redshift can then be described as a result of increased damping. Different channels of attenuation can also be discerned with the power  $p$  of  $\lambda^p$  dependence of absorption at the lower wavelength slope: 1.5 corresponds to acoustic phonon scattering, 2 – to electron–electron scattering, 2.5 – to interaction with optical phonons, 3–3.5 – with ionized impurity defects.<sup>16</sup> Our observations suggest that the role of phonon

scattering is significant in case of plasmonic silicon nanocrystals. Therefore, a frequency-dependent  $\Gamma$  should be assumed. Construction of a theoretically sound function accounting for different power law dependences of separate damping channels as well as for screened plasma frequency (similar to that described in ref. 49) would require much more detailed sampling, so an empirical approach was adopted. The model assuming sigmoidal shape of  $\Gamma(\omega)$ <sup>5</sup> was introduced. Alternatively, similar frequency variation of the damping term may be obtained by considering intraband transitions with use of Drude–Smith model.<sup>50</sup> The background for the approach to fit experimental IR spectra is discussed in more detail in Section S.IV of the ESI.† The results of IR spectra approximation are present in Fig. 4.  $\omega_P$  was found to be 5500, 5600 and 3700  $\text{cm}^{-1}$  for samples Si\_9.1, Si\_20 and Si\_36, respectively.

Free carrier concentration in SNPs is extracted from  $\omega_P$  value with following equation:<sup>9–11,49</sup>

$$\omega_P = \sqrt{\frac{N_c e^2}{m^* \epsilon_0}} \quad (4)$$

where  $N_c$  is the free carrier concentration in SNPs,  $e$  – the elementary charge,  $m^*$  – the effective mass of charge carriers,  $\epsilon_0$  – the vacuum permittivity. The use of effective mass approximation to describe electronic excitations in SNPs has been proven adequate with both *ab initio* calculations and experimental results for particles with  $R > 2$  nm.<sup>8,51</sup> Using extracted  $\omega_P$  frequencies and assuming  $m^* = 0.26 m_e$ , where  $m_e$  is the electron rest mass, one can estimate  $N_c$  values of  $8.8 \times 10^{19}$ ,  $9.1 \times 10^{19}$  and  $4.0 \times 10^{19} \text{ cm}^{-3}$  for Si\_9.1, Si\_20 and Si\_36 samples. The same values normalized to volumetric atomic concentration of phosphorus in SNPs result in the net carrier generation efficiency  $\eta$  of 7.0, 4.5 and 0.8%. This clearly shows that a major portion of the impurity is inactive. We associate this fact firstly with excessive phosphorus content in the natural oxide layer. Indeed, with an initial step of SNPs wet etching with HF the impurity content drastically decreases (Table 1). On the contrary, the position of LSPR band blueshifts, which results in  $\eta$  rising up to 34%. This value is, to the best of our knowledge, unprecedented for Si SNPs.

It is worth noting that inactive excess phosphorus at the interface may also trap charge carriers, as we observe lower  $\eta$  values for samples with higher impurity content. Possibility of acceptor behavior of phosphorus in oxide-embedded P-doped Si nanocrystals was demonstrated with X-ray absorption near edge structure spectroscopy.<sup>52</sup>

Plasmonic behavior of SNPs can provide even deeper insight into distribution of an impurity within the particles. As IR spectroscopy requires only a small amount of the material, studies of up to 4 steps of sequential etching were accomplished (Fig. 6). Observed variation in  $\omega_P$  can be well explained with carrier trapping. Existence of LSPR in SNPs is often connected to the surface/interface quality in terms of concentration of trap states.<sup>9,13</sup> HF etching is known to efficiently reduce the surface concentration of  $P_b$  centers at Si/SiO<sub>x</sub> interface,<sup>37</sup> which accounts for the increased  $N_c$  on the initial etching step. A gradual decrease of  $\omega_P$  with further etching steps is then



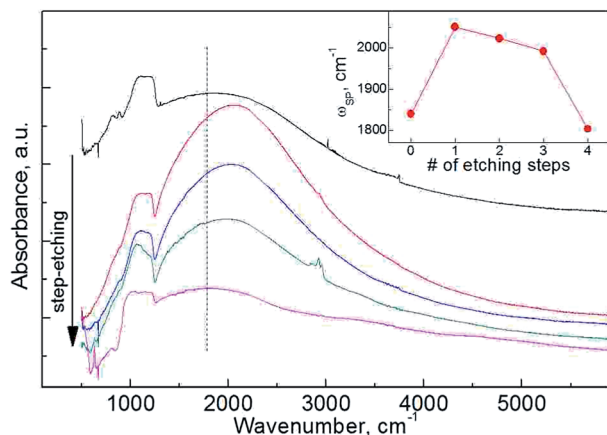


Fig. 6 Evolution of LSPR absorption band of sample Si<sub>36</sub> during the step-etching process, as-synthesized sample and 4 steps of HF etch are shown. The spectra are offset vertically for clarity and normalized for areal intensity of SiO<sub>x</sub> group vibration features. Dashed vertical line denotes the original position of maximum of LSPR band and is a guide for the eye. Inset – the position of LSPR band maximum as a function of number of etching steps.

ascribed to an increase of surface-to-volume ratio of the particles.

As plasmonic response is present for all the etched samples we can conclude that phosphorus diffuses deep into the nanoparticles' cores. LSPR band evolution with step etching and HAADF-STEM elemental mapping are consistent with uniform radial distribution of phosphorus in silicon cores.

Thus the proposed diffusion doping technique provides valuable doping levels of SNPs with high generation efficiency to induce multiple in-particle carrier generation for LSPR response.

Doped SNPs with well-controlled size and impurity position distribution are desired for construction of devices. This is most evident when examining transport properties of SNPs. Monodisperse particles show enhanced conductivity in a nanocrystalline superlattice due to propagation of delocalized states.<sup>53</sup> Contrarily, polydispersity leads to emergence of Anderson localization regime.<sup>1</sup> Single impurities have been shown to give rise to backscattering in silicon nanowires, with variance in impurity position potentially leading to a drop of conduction in large energy window.<sup>45</sup> Decomposition of silane, which is currently the most prominent method of synthesis of doped Si SNPs, naturally leads to polydisperse ensembles of particles. At the same time, post-synthetic diffusion doping may be easily coupled with techniques capable of producing monodisperse Si SNPs (*e.g.* decomposition of hydrogen silsesquioxane<sup>54</sup>), high-throughput techniques like plasma chemical synthesis from condensed phase,<sup>55</sup> low-cost ball milling techniques.<sup>56,57</sup>

## IV Conclusions

We have described a simple technique for diffusion doping of Si SNPs with phosphorus from a gaseous phase. Phosphorus vapor pressure was established as a main parameter for quantitative

control of SNPs' DLs up to 10% at. According to EDX elemental mapping the method results in rather uniform distribution of phosphorus in the ensemble, providing equivalent doping of silicon SNPs. Highly doped nanoparticles exhibit well-pronounced thermoelectric and plasmonic properties proving implantation of P into nanocrystalline silicon cores. The particles are air-stable, providing no shift of plasmonic frequencies in time due to natural oxide shell. Fitting of LSPR allowed to determine free carrier concentrations exceeding  $10^{20} \text{ cm}^{-3}$  with dopant activation efficiencies up to 34%. Temperature dependence of LSPR and its lineshape also confirmed significance of electron-phonon interaction in plasmonic Si SNPs, which can become a potential bottleneck for shifting the LSPR band position towards the visible part of the spectrum.

In conjunction with etching the technique can provide a great variety of P radial profiles in Si SNPs. This may prove useful in characterization of the influence of impurity position on the properties of nanoparticles, such as LSPR and thermopower, as well as in tuning thereof. The technique is potentially beneficial for n-type doping of SNPs with other group 15 elements (As, Sb) providing suitable precursors with high enough vapor pressure.

## Conflicts of interest

There are no conflicts of interest to declare.

## Acknowledgements

This work was supported by Russian Foundation for Basic Research grant No 17-03-01269. The authors acknowledge (partial) support from M. V. Lomonosov Moscow State University Program of Development.

## References

- 1 D. V. Talpin and C. B. Murray, *Science*, 2005, **310**, 86.
- 2 J. Jang, D. S. Dolzhenkov, W. Liu, S. Nam, M. Shim and D. V. Talpin, *Nano Lett.*, 2015, **15**, 6309.
- 3 J. van Embden, A. S. R. Chesman, E. Della Gaspera, N. W. Duffy, S. E. Watkins and J. J. Jasieniak, *J. Am. Chem. Soc.*, 2014, **136**, 5237.
- 4 R. Lechner, H. Wiggers, A. Ebbers, J. Steiger, M. S. Brandt and M. Stutzmann, *Phys. Status Solidi RRL*, 2007, **1**, 262.
- 5 I. Kriegel, J. Rodríguez-Fernández, A. Wisnet, H. Zhang, C. Waurisch, A. Eychmüller, A. Dubavik, A. O. Govorov and J. Feldmann, *ACS Nano*, 2013, **7**, 4367.
- 6 R. Lechner, A. R. Stegner, R. N. Pereira, R. Dietmueller, M. S. Brandt, A. Ebbers, M. Trocha, H. Wiggers and M. Stutzmann, *J. Appl. Phys.*, 2008, **104**, 053701.
- 7 J. A. Fauchaux, A. L. D. Stanton and P. K. Jain, *J. Phys. Chem. Lett.*, 2014, **5**, 976.
- 8 X. Pi and C. Delerue, *Phys. Rev. Lett.*, 2013, **111**, 177402.
- 9 S. Zhou, X. Pi, Z. Ni, Y. Ding, Y. Jiang, C. Jin, C. Delerue, D. Yang and T. Nozaki, *ACS Nano*, 2015, **9**, 378.
- 10 D. J. Rowe, J. S. Jeong, K. A. Mkhoyan and U. R. Kortshagen, *Nano Lett.*, 2013, **13**, 1317.



- 11 S. Zhou, Z. Ni, Y. Ding, M. Sugaya, X. Pi and T. Nozaki, *ACS Photonics*, 2016, **3**, 415.
- 12 S. Zhou, X. Pi, Z. Ni, Q. Luan, Y. Jiang, C. Jin, T. Nozaki and D. Yang, *Part. Part. Syst. Charact.*, 2015, **32**, 213.
- 13 N. J. Kramer, K. S. Schramke and U. R. Kortshagen, *Nano Lett.*, 2015, **15**, 5597.
- 14 M. R. Scriba, D. T. Britton and M. Härting, *Thin Solid Films*, 2011, **519**, 4491.
- 15 X. D. Pi, R. Gresback, R. W. Liptak, S. A. Campbell and U. Kortshagen, *Appl. Phys. Lett.*, 2008, **92**, 123102.
- 16 A. Mimura, M. Fujii, S. Hayashi, D. Kovalev and F. Koch, *Phys. Rev. B*, 2000, **62**, 12625.
- 17 M. Perego, G. Seguini and M. Fanciulli, *Surf. Interface Anal.*, 2013, **45**, 386.
- 18 H. Gnaser, S. Gutsch, M. Wahl, R. Schiller, M. Kopnarski, D. Hiller and M. Zacharias, *J. Appl. Phys.*, 2014, **115**, 034304.
- 19 T. Makimura, Y. Yamamoto, S. Mitani, T. Mizuta, C. Q. Li, D. Takeuchi and K. Murakami, *Appl. Surf. Sci.*, 2002, **197–198**, 670.
- 20 L. Tsybeskov, K. D. Hirschman, S. P. Dutttagupta, M. Zacharias, P. M. Fauchet, J. P. McCaffrey and D. J. Lockwood, *Appl. Phys. Lett.*, 1998, **72**, 43.
- 21 G.-R. Lin, C.-J. Lin and H.-C. Kuo, *Appl. Phys. Lett.*, 2007, **91**, 093122.
- 22 I. Perez-Wurfl, X. Hao, A. Gentle, D.-H. Kim, G. Conibeer and M. A. Green, *Appl. Phys. Lett.*, 2009, **95**, 153506.
- 23 G.-R. Lin, Y.-H. Pai, C.-T. Lin and C.-C. Chen, *Appl. Phys. Lett.*, 2010, **96**, 263514.
- 24 N. P. Lyakishev, *State diagrams of double metallic systems*, Mashinostroyeniye, Moscow, 2001.
- 25 Z. Ni, X. Pi and D. Yang, *Phys. Rev. B*, 2014, **89**, 035312.
- 26 A. Carvalho, S. Öberg, M. Barroso, M. J. Rayson and P. Briddon, *Phys. Status Solidi A*, 2012, **209**, 1847.
- 27 R. Guerra and S. Ossicini, *J. Am. Chem. Soc.*, 2014, **136**, 4404.
- 28 M. Perego, G. Seguini, E. Arduca, J. Frascaroli, D. de Salvador, M. Mastromatteo, A. Carnera, G. Nicotra, M. Scuderi, C. Spinella, G. Impellizzeri, C. Lenardi and E. Napolitani, *Nanoscale*, 2015, **7**, 14469.
- 29 F. Ruffino, L. Romano, E. Carria, M. Miritello, M. G. Grimaldi, V. Privitera and F. Marabelli, *J. Nanotechnol.*, 2012, **2012**, 635705.
- 30 G. A. Kachurin, S. G. Yanovskaya, D. I. Tetelbaum and A. N. Mikhaylov, *Phys. Tech. Semicond.*, 2003, **37**, 738.
- 31 P. G. Kik, M. L. Brongersma and A. Polman, *Appl. Phys. Lett.*, 2000, **76**, 2325.
- 32 N. N. Kononov, G. P. Kuz'min, A. N. Orlov, O. V. Tikhonevitch and A. A. Surkov, *Phys. Tech. Semicond.*, 2005, **39**, 868.
- 33 I. S. Grigor'ev and E. Z. Mejlihov, *Physical values*, Energoatomizdat, Moscow, 1991.
- 34 L. V. Myshlyayeva and V. V. Krasnoschokov, *Analytical chemistry of silicon*, Nauka, Moscow, 1972.
- 35 P. L. Buldini and D. Sandrini, *Anal. Chim. Acta*, 1978, **98**, 401.
- 36 V. Petricek, M. Dusek and L. Palatinus, *Z. Kristallogr.*, 2014, **229(5)**, 345.
- 37 S. Niesar, A. R. Stegner, R. N. Pereira, M. Hoeb, H. Wiggers, M. S. Brandt and M. Stutzmann, *Appl. Phys. Lett.*, 2010, **96**, 193112.
- 38 J. E. Smith Jr., M. H. Brodsky, B. L. Crowder and M. I. Nathan, *Phys. Rev. Lett.*, 1971, **26**, 642.
- 39 N. H. Nickel, P. Lengsfeld and I. Sieber, *Phys. Rev. B*, 2000, **61**, 15558.
- 40 U. Fano, *Phys. Rev.*, 1961, **124**, 1866.
- 41 K. H. Khoo, A. T. Zayak, H. Kwak and J. R. Chelikowsky, *Phys. Rev. Lett.*, 2010, **105**, 115504.
- 42 H. Richter, Z. P. Wang and L. Ley, *Solid State Commun.*, 1981, **39**, 625.
- 43 W. Kim and A. Majumdar, *J. Appl. Phys.*, 2006, **99**, 084306.
- 44 K. H. Khoo and J. R. Chelikowsky, *Phys. Rev. B*, 2014, **89**, 195309.
- 45 M.-V. Fernández-Serra, C. Adessi and X. Blase, *Nano Lett.*, 2006, **6**, 2674.
- 46 R. J. Mendelsberg, G. Garcia, H. Li, L. Manna and D. J. Milliron, *J. Phys. Chem. C*, 2012, **116**, 12226.
- 47 C. F. Bohren and D. R. Huffman, *Absorption and Scattering of Light by Small Particles*; Wiley-VCH: Weinheim, 2004.
- 48 S. Link and M. A. El-Sayed, *J. Phys. Chem. B*, 1999, **103**, 4212.
- 49 J. Ederth, P. Johnsson, G. A. Niklasson, A. Hoel, A. Hultåker, P. Heszler, C. G. Granqvist, A. R. van Doorn, M. J. Jongerius and D. Burgard, *Phys. Rev. B*, 2003, **68**, 155410.
- 50 H. Zhang, R. Zhang, K. S. Schramke, N. M. Bedford, K. Hunter, U. R. Kortshagen and P. Nordlander, *ACS Photonics*, 2017, **4**, 963.
- 51 T.-L. Chan, M. L. Tiago, E. Kaxiras and J. R. Chelikowsky, *Nano Lett.*, 2008, **8**, 596.
- 52 D. König, S. Gutsch, H. Gnaser, M. Wahl, M. Kopnarski, J. Gottlicher, R. Steininger, M. Zacharias and D. Hiller, *Sci. Rep.*, 2015, **5**, 9702.
- 53 S. Xu, D. Thian, S. Wang, Y. Wang and F. B. Prinz, *Phys. Rev. B*, 2014, **90**, 144202.
- 54 M. Dasog, Z. Yang, S. Regli, T. M. Atkins, A. Faramus, M. P. Singh, E. Muthuswamy, S. M. Kauzlarich, R. D. Tilley and J. G. C. Veinot, *ACS Nano*, 2013, **7**, 2676.
- 55 I. A. Tutorskii, A. I. Belogorokhov, A. A. Ishchenko and P. A. Storozhenko, *Colloid J.*, 2005, **67**, 491.
- 56 Y. Jin, S. Zhang, B. Zhu, Y. Tan, X. Hu, L. Zong and J. Zhu, *Nano Lett.*, 2015, **15**, 7742.
- 57 L. Zong, Y. Lin, C. Liu, B. Zhu, X. Hu, Z. Lu and J. Zhu, *Nano Lett.*, 2016, **16**, 7210.

